Adaptive pathfinding by nucleokinesis during amoeboid migration

Janina Kroll[1], Robert Hauschild[2], Artur Kuznetcov[1], Kasia Stefanowski[1], Monika D Hermann[1], Jack Merrin[2], Lubuna Shafeek[2], Annette Müller-Taubenberger[3] & Jörg Renkawitz[1,*]

Abstract

Motile cells encounter microenvironments with locally heterogeneous mechanochemical composition. Individual compositional parameters, such as chemokines and extracellular matrix pore sizes, are well known to provide guidance cues for pathfinding. However, motile cells face diverse cues at the same time, raising the question of how they respond to multiple and potentially competing signals on their paths. Here, we reveal that amoeboid cells require nuclear repositioning, termed nucleokinesis, for adaptive pathfinding in heterogeneous mechanochemical microenvironments. Using mammalian immune cells and the amoeba *Dictyostelium discoideum*, we discover that frequent, rapid and long-distance nucleokinesis is a basic component of amoeboid pathfinding, enabling cells to reorientate quickly between locally competing cues. Amoeboid nucleokinesis comprises a two-step polarity switch and is driven by myosin-II forces that readjust the nuclear to the cellular path. Impaired nucleokinesis distorts path adaptions and causes cellular arrest in the microenvironment. Our findings establish that nucleokinesis is required for amoeboid cell navigation. Given that many immune cells, amoebae, and some cancer cells utilize an amoeboid migration strategy, these results suggest that nucleokinesis underlies cellular navigation during unicellular biology, immunity, and disease.

Introduction

The ability of cells to navigate their path while moving themselves forward is critical for innate and adaptive immune responses, organismal development, tissue maintenance, and single-cell organisms. During navigational migration, cells are surrounded by local environments that are composed of extracellular matrix, interstitial fluid, and tissue cells in the case of cellular migration in multicellular organisms, or natural environments like soil in the case of motile single-cell organisms. To efficiently navigate through these environments, migrating cells are equipped with mechanisms to follow diverse chemical as well as mechanical cues (Charras & Sahai, 2014; Moreau *et al*, 2018; van Helvert *et al*, 2018; Yamada & Sixt, 2019). Most well investigated are chemotactic signals like chemokines, which are detected by the respective cellular receptors and align intracellular force generation by the actin cytoskeleton toward the chemotactic cue, such as during the recruitment of immune cells to sites of inflammation or into lymphatics (Nourshargh & Alon, 2014; Hauser *et al*, 2016; Worbs *et al*, 2017). Yet at the same time, motile cells also encounter mechanical guidance cues along their paths, such as differently sized pores in the extracellular matrix (Wolf *et al*, 2013; Renkawitz *et al*, 2019).

Navigating motile cells frequently generate new protrusions ("leading edges"; "cell fronts") next to preexisting ones, followed by a preference for one of the protrusions, along which the path of migration is subsequently orientated. This morphological characteristic of multiple simultaneous protrusions is particularly common in shallow chemotactic gradients (Gerisch & Keller, 1981; Swanson & Taylor, 1982; Andrew & Insall, 2007; Kay *et al*, 2008), suggesting that cells employ these multiple protrusions to sense chemotactic cues at different micro-locations in their immediate surrounding. This notion is supported by the observation that deficiency of the Arp2/3 regulator Hem1 in motile immune cells not only reduces protrusion formation but also impairs migration along chemotactic gradients (Leithner *et al*, 2016). Collectively, these findings suggest that cells utilize alternative protrusions to simultaneously explore and measure guidance cues at different local sites in their immediate microenvironment. These explorative protrusions are most evident in fast-migrating amoeboid cells, such as neutrophils and dendritic cells, which adopt highly dynamic and ramified cell shapes (Fritz-Laylin *et al*, 2017; Driscoll *et al*, 2019; Renkawitz *et al*, 2019). While some principles of how migrating cells coordinate these complex cell shapes have been identified (Devreotes *et al*, 2017; Kopf *et al*, 2020; Hadjitheodorou *et al*, 2021, 2023), it remains entirely unknown how motile cells deal with locally diverse and potentially

1   Biomedical Center Munich (BMC), Walter Brendel Center of Experimental Medicine, Institute of Cardiovascular Physiology and Pathophysiology, University Hospital, Ludwig Maximilians University Munich, Munich, Germany
2   Institute of Science and Technology Austria, Klosterneuburg, Austria
3   Biomedical Center Munich (BMC), Department of Cell Biology (Anatomy III), Ludwig Maximilians University Munich, Munich, Germany
    *Corresponding author. Tel: + 49 089 2180 71516; E-mail: joerg.renkawitz@med.uni-muenchen.de

competing mechanochemical inputs, and how they reorganize their intracellular content along the dominant protrusion once a path has been selected.

Here, we address these open questions by investigating how amoeboid cells navigate their path in locally heterogeneous microenvironments. We identify thresholds at which chemical chemokine cues overrule mechanical pore size cues and vice versa. Furthermore, we reveal that protrusions extending through larger extracellular pores often contain the nucleus, necessitating rapid and large-distant intracellular repositioning of the nucleus, when the cell decides to follow a path defined by an emerging stronger chemotactic cue. Active intracellular relocation of the nucleus to specific intracellular locations is known to occur in various model systems, including neurons and multinuclear muscle cells (Gundersen & Worman, 2013), and has been termed "nucleokinesis." Yet, how amoeboid migrating cells position their nucleus by nucleokinesis to align the nuclear path to the cellular path, despite their high shape dynamics, fast migration velocity, and unusual forward position of the nucleus in front of the MTOC (microtubule-organizing center), remained unknown. Here, we identify nucleokinesis during amoeboid migration, elucidate its mechanistic basis, and uncover its role in adaptive pathfinding within microenvironments characterized by competing chemical and physical cues.

Results

Rapid and long-distance nucleokinesis during amoeboid immune cell migration

As a model system for cell migration in microenvironments of heterogeneous mechanochemical composition, we imaged dendritic cells migrating along a chemotactic gradient (CCL19) while being embedded in a three-dimensional collagen matrix composed of varying pore sizes (Wolf *et al*, 2013; Schwarz *et al*, 2017; Driscoll *et al*, 2019; Renkawitz *et al*, 2019). Migrating dendritic cells frequently showed a ramified cell shape with multiple protrusions, continuously generating new protrusions next to existing ones and eventually favoring one protrusion to select the preferred path of migration (Fig 1A and B, and Movie EV1). In line with the function of the nucleus to act as a mechanical ruler to guide migration along the path of larger pore sizes (Renkawitz *et al*, 2019; Lomakin *et al*, 2020; Venturini *et al*, 2020), the cellular path was frequently identical with the nuclear path (Fig 1B). Yet, in one out of four path decisions we observed mispositioning of the nucleus into future 'losing' protrusions (Fig 1C and D). This deviation of the nuclear path from the cellular path caused a subsequent long-distance repositioning of the entire nucleus toward the winning protrusion, effectively realigning the nuclear with the cellular path (Movie EV1). Additionally, we also often observed repositioning of only parts of the nucleus, when the nucleus itself deformed simultaneously towards alternative cell protrusions, without entirely locating into these protrusions. In these situations, only the subnuclear part (nuclear protrusion) locating inside the "losing" protrusion had to be repositioned towards the "winning" protrusion along the selected cell path (Fig 1C and Movie EV1).

The intracellular repositioning of the entire nucleus relative to the cell body, also called nucleokinesis (Tsai & Gleeson, 2005;

Gundersen & Worman, 2013), was very rapid with velocities of 2–9 μm/min (Fig 1F and Appendix Fig S1A) and displayed rapid accelerations faster than the movement of the cell body (Fig 1H). Nucleokinesis occurred approximately once per hour during DC migration within collagen matrices (Fig 1E) and over long intracellular distances of up to 45 μm (Fig 1G and Appendix Fig S1A–C). To test whether nucleokinesis is a general feature of amoeboid immune cell migration, we imaged T cells, which have a smaller and less-branched cytoplasmic cell body, and still detected frequent and rapid repositioning of the entire nucleus from "losing" into winning protrusions (Fig 1D–I and Movie EV3). These findings identify nucleokinesis as a novel component of amoeboid immune cell migration.

Nucleokinesis enables adaptive pathfinding in competing chemokine and pore size cues

As migrating cells encounter chemical (e.g., chemokine gradients) as well as mechanical (e.g., varying pores sizes) cues at the same time (Moreau *et al*, 2018; Yamada & Sixt, 2019; Kameritsch & Renkawitz, 2020), our observations suggested that cells may use nucleokinesis to flexibly adapt their path between locally competing guidance cues. To functionally test this hypothesis, we engineered reductionistic cellular path decision points, at which migrating cells encounter two path options with different strengths of chemotactic as well as pore size cues. To provide diverse pore size cues, we generated two differently sized pores at the path junction, with pore sizes ranging from 8 to 2 μm width. According to the previously described mechanism for sensing pore sizes (Renkawitz *et al*, 2019), migrating cells did not differentiate between large 8 and 6 μm pores but when choosing between a small pore (2 or 4 μm) and a large 8 μm pore (Figs 2A and EV1A). Next, to test whether we can selectively guide cells towards a specific path based on a stronger chemokine cue, we engineered one path to be closer to the source of the chemokine than the alternative path, which follows a snake-like pattern and thus is more distant to the chemokine source (Fig 2B). Simulation of the diffusion of the chemotactic gradient over time showed that the snake-like path indeed causes higher chemokine concentrations at the path junction towards the path closer to the chemokine source (Fig EV1B). We confirmed these results experimentally by visualizing the chemotactic gradient by using fluorescent 10 kDa dextran as a proxy for the chemokine CCL19, showing stably higher concentrations over time at the path junction towards the path closer to the chemokine source and lower concentrations towards the path more distant to the chemokine source (Fig 2B).

Next, we investigated cellular decisions upon offering both chemokine and mechanical cues simultaneously at single path junctions (Fig 2C–E). When both paths were composed of almost equally sized large pores at their entrances, exceeding the threshold of the nuclear pore size sensing mechanism, cells showed a strong preference for the path closer to the chemokine source (Fig 2C and F, and Movie EV2). Yet, when we gradually narrowed the entrance pore of chemokine-proximal path, cells increasingly favored the alternative path, which was more distant to the chemokine source but had a larger pore at the path entrance (Fig 2C–H and Movie EV2). In contrast, in the absence of a chemokine source, cells always preferentially selected the longer paths with wider pores (Fig EV1C–E). Thus, these findings reveal that chemokine and pore
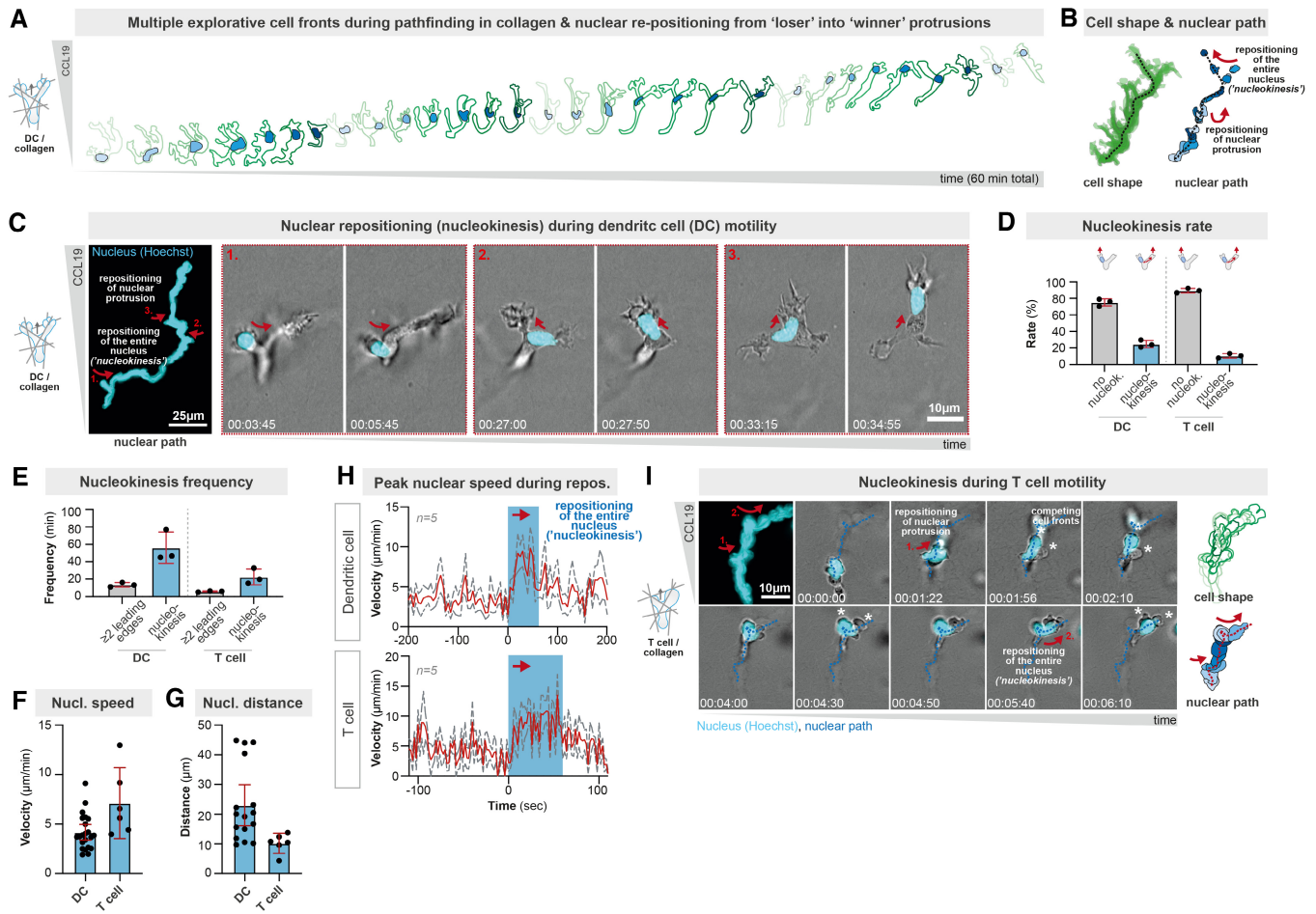
Figure 1. Immune cells employ rapid and long-distance nucleokinesis during amoeboid cell migration.

A   Cellular outlines (shades of green, time color-coded) of a representative bone marrow-derived mouse dendritic cell (DC) migrating in a three-dimensional collagen matrix along a CCL19 chemokine gradient. The intracellular localization of the DC nucleus during pathfinding is shown in blue (shades of blue, time color-coded). See also Movie EV1.

B   Projection cellular (green) and nuclear (blue) path of the cell in (A) over 60 min time. Note the two events, in which either only parts of the nucleus (nuclear protrusions) or the entire nucleus deviate from the cellular path, the later requiring full intracellular nuclear repositioning (called "nucleokinesis").

C   Representative nucleokinesis events in a bone marrow-derived DC migrating through a three-dimensional collagen matrix along a CCL19 chemokine gradient. Highlights in dashed boxes show events of repositioning of the entire nucleus (1., "nucleokinesis") or parts of the nucleus (2. & 3., "nuclear protrusions"). Time in h:min:s.

D   Quantification of the rate of nucleokinesis events in amoeboid DCs and T cells migrating in a collagen matrix: when the migrating cell has a least two major protrusions, quantification of whether the nucleus locates immediately into the dominant protrusion or first locates into the future retracting protrusion, requiring nucleokinesis into the future dominant protrusion. Data are mean ± SD. N = 31 DCs (3 replicates, 135 events) and 30 T cells (3 replicates, 100 events).

E   Quantification of how often (frequency) DCs and T cells have multiple simultaneous protrusions and how often they show nucleokinesis events in a collagen matrix: as in (D), but showing the frequency of at least two clearly observable leading edges and nucleokinesis events per minute. Data are mean ± SD. N = 31 DCs (3 replicates, 135 events) and 30 T cells (3 replicates, 100 events).

F   Quantification of the speed of nuclear movement during full nucleokinesis in DCs and T cells. N = 16 DCs (3 replicates), 6 T cells (3 replicates). Data are median ± 95CI.

G   Quantification of the intracellular distance of nuclear movement during full nucleokinesis in DCs and T cells. N = 16 DCs (3 replicates), 6 T cells (3 replicates). Data are median ± 95CI.

H   Measurements of nuclear speed before, during, and after full nucleokinesis events in DCs and T cells. The blue box marks the nucleokinesis event. Data are mean ± SEM (the mean is shown as a red line and the SEM is shown as dashed gray lines). N = 5 cells.

I   Representative nucleokinesis events in a T cell migrating through a three-dimensional collagen matrix along a CCL19 chemokine gradient. Red arrows highlight events of repositioning of the parts of the nucleus (1., "nuclear protrusions") or the entire nucleus (2., "nucleokinesis"). Time projections of the cellular and nuclear paths are shown in shades of green and blue, respectively. Time in h:min:s.

Source data are available online for this figure.

size cues are competitive and identify thresholds at which chemokine cues overrule pore size cues and vice versa.

To test for the functional relevance of nucleokinesis, we imaged the spatiotemporal dynamics of nuclear behavior during these path decisions. While the nucleus was often immediately positioned in the future winning protrusion, we also observed frequent nucleokinesis events in which the nucleus was mispositioned far-distantly into the future "wrong" path, necessitating long-distance nucleokinesis to the "winning" protrusion (Fig 2I–L and Movie EV2). Notably, nucleokinesis occurred particularly frequently when the nucleus
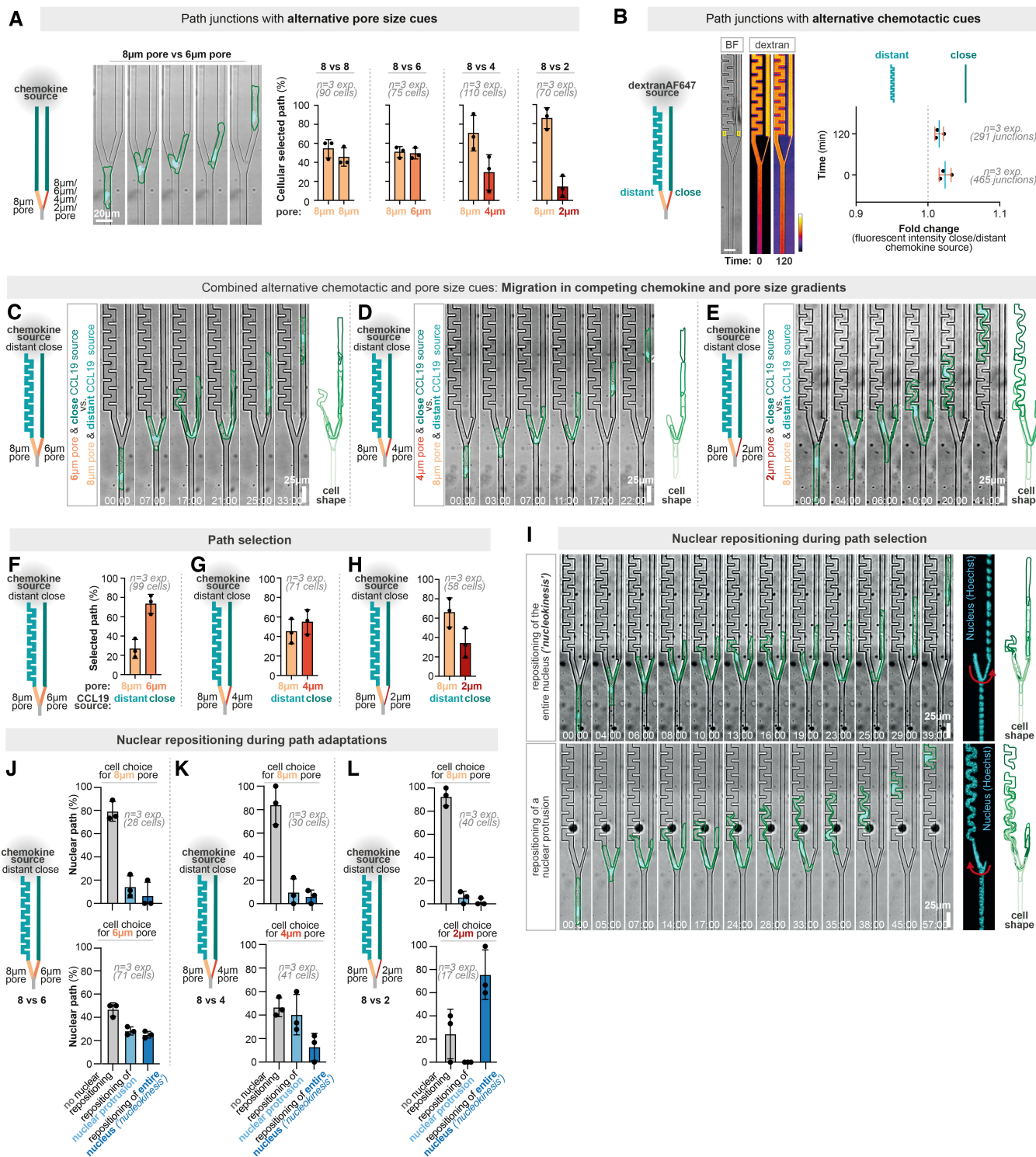

Figure 2.

Figure 2. Nucleokinesis enables adaptive pathfinding in competing chemokine and pore size cues.

A Left: Representative bone marrow-derived DCs (BMDC) migrating in microchannels with two-way path junctions with different pores but an equally long and symmetric path towards the chemokine source sizes (8 vs. 6 μm shown here; representative examples for 8 vs. 8, 8 vs. 4, or 8 vs. 2 μm are shown in Fig EV1A). The cell shape is outlined in green and the nucleus is visualized by Hoechst (cyan). Right: quantification of cellular path decisions. *N* = 3 replicates (90 cells for 8 vs. 8 μm decisions; 75 cells for 8 vs. 6 μm decisions; 110 cells for 8 vs. 4 μm decisions; 70 cells for 8 vs. 2 μm decisions). Data are Mean ± SD.

B Visualization and quantification of 10 kDa dextran-AF647 gradients as a proxy for the similarly sized chemokine CCL19. DextranAF647 (fire-color coded) was added with CCL19 to the loading source hole and its diffusion was visualized by fluorescent microscopy over time. The experiment was performed in the presence of bone-marrow-derived DCs (BMDCs). The yellow rectangles mark the area of quantitative measurements of dextraneAF647 concentrations. *N* = 3 replicates (465 and 291 junctions at timepoints 0 and 120, respectively). Timepoint 0 represent the timepoint when the cells started to migrate into PDMS devices. Data are Mean ± SD.

C Representative bone marrow-derived dendritic cell (DC) approaching a path junction with two alternative path options and competing chemokine and pore size cues: the left path has an 8-μm wide pore, but is more distantly located to the CCL19 chemokine source. The right path has a 6-μm wide pore and is more closely located to the CCL19 chemokine source. The cell shape is outlined in green and the nucleus is visualized by Hoechst (cyan). Time in min:s.

D As in (C), but the right path that is closer to the chemokine source has a pore size of only 4 μm.

E As in (C), but the right path that is closer to the chemokine source has a pore size of only 2 μm.

F Quantification of cellular path decisions in the microenvironments shown in (C). See also Fig EV1C for controls without a chemokine source. Data are Mean ± SD. *N* = 3 replicates (99 cells).

G Quantification of cellular path decisions in the microenvironments shown in (D). See also Fig EV1D for controls without a chemokine source. Data are Mean ± SD. *N* = 3 replicates (71 cells).

H Quantification of cellular path decisions in the microenvironments shown in (E). See also Fig EV1E for controls without a chemokine source. Data are Mean ± SD. *N* = 3 replicates (58 cells).

I Representative full and partial nucleokinesis events during cellular path decisions in the competing chemokine and pore sizes cues. The cell shape is outlined in green and the nucleus is visualized by Hoechst (cyan). Time in min:s.

J Quantification of nucleokinesis events in the microenvironments shown in (C), depending on whether the cell finally decides for the larger 8-μm or smaller 6-μm pore. Data are Mean ± SD. *N* = 3 replicates (40 cells or 17 cells with the final decision either for 8- or 6-μm pore, respectively).

K Quantification of nucleokinesis events in the microenvironments shown in (D), depending on whether the cell finally decides for the larger 8-μm or smaller 4-μm pore. Data are Mean ± SD. *N* = 3 replicates (30 cells or 41 cells with the final decision either for 8- or 4-μm pore, respectively).

L Quantification of nucleokinesis events in the microenvironments shown in (E), depending on whether the cell finally decides f or the larger 8-μm or smaller 2-μm pore. Data are Mean ± SD. *N* = 3 replicates (28 cells or 71 cells with the final decision either for 8- or 2-μm pore, respectively).

Source data are available online for this figure.

was initially positioned into the path bearing a larger pore entrance, but the cell selected the alternative path with a narrow pore entrance with a stronger chemotactic cue (Fig 2J–L). These findings show that cells can overcome the nuclear pore size sensing mechanism by chemotactic inputs and that nucleokinesis is required to adapt the nuclear path to the cellular path along an appearing dominating cue. Thus, nucleokinesis enables adaptive pathfinding during amoeboid cell navigation to flexibly navigate along locally competing mechanochemical guidance cues.

Two-step amoeboid nucleokinesis by consecutive cell polarity switches

It is well established that cytoskeletal forces are able to intracellularly move and position the nucleus in diverse cell types such as neurons, glial cells, muscle cells, and fibroblasts (Gundersen & Worman, 2013; Cadot *et al*, 2015; Calero-Cuenca *et al*, 2018). Plotting the speed and distance of nucleokinesis in these cell types in comparison to the here measured parameters revealed an extraordinary efficiency of nucleokinesis in immune cells, being rapid as well as far distant (Appendix Fig S1A). Notably, the intracellular behavior of the immune cell's nucleus was reminiscent of the amoeboid's cell body behavior, meaning that the nucleus moved rapidly, flexibly, and with continuous shape changes (e.g., Fig 1C and Movie EV1). As these parameters are hallmarks of amoeboid cell behavior, we propose to name nucleokinesis in amoeboid cells as "amoeboid nucleokinesis".

To unravel the mechanistic basis of amoeboid nucleokinesis, we next imaged the spatiotemporal dynamics of the centrosome-to-nucleus axis, an important indicator of cell polarity and cytoskeletal forces acting on the nucleus during nuclear movement (Luxton &

Gundersen, 2011). To uncouple nucleokinesis from effects caused by cellular squeezing, we established novel path junctions with equally large pore sizes but one blocked path, causing nucleokinesis events from the blocked to the open path (Fig 3A, Appendix Fig S2A–D, and Movie EV3). Using EB3-mCherry expressing DCs as a marker for the centrosome (also called microtubule-organizing center (MTOC)) and semi-automated imaging analysis (Appendix Fig S2E), we observed two rapid polarity switches in the nucleus-MTOC axis configuration during amoeboid nucleokinesis (Fig 3A and Movie EV3): while DCs migrated with a typical amoeboid nucleus-forward configuration (Renkawitz *et al*, 2019) before nucleokinesis (Fig 3A–C), the repositioning of the nucleus from the "losing" into the "winning" protrusion coincided with a switch in the nucleus-MTOC axis configuration as the cells moved with the MTOC in front of the nucleus during the first phase of nucleokinesis (Fig 3A–C). When the DCs continued their path of migration after the first phase of nucleokinesis, the nucleus passed again the MTOC to restore the initial nucleus-MTOC axis configuration (Fig 3A–C), showing that the nucleus does not passively stay at the cell rear upon the retraction of the nucleus-containing "losing" protrusion, but actively repositions to its original location frontward of the MTOC during the second phase of nucleokinesis (Fig EV2A). Together, these data show that nucleokinesis in migrating amoeboid cells is composed of two phases: in the first phase of nucleokinesis, the nucleus travels intracellularly from the "losing" into the "winning" protrusion. In the second phase of nucleokinesis, the nucleus travels from the rear of the MTOC to the front of the MTOC.

To corroborate these findings, we used the microtubule markers EMTB-mCherry and Spy-tubulin as additional MTOC markers (Fig EV2B and C), as well as manual mapping of the MTOC-to-nucleus axis during nucleokinesis (Fig EV2D–F), confirming both

observed rapid polarity switches (Appendix Fig S3A–F) during the first and second phases of amoeboid nucleokinesis. Similarly, when we investigated the MTOC-to-nucleus axis during DC pathfinding in deformable collagen networks, we observed preferential MTOC-forward configuration during the first phase of nucleokinesis, followed by the restoration of the nucleus-forward configuration during the second phase of nucleokinesis (Fig 3D and E). Together, these findings identify that amoeboid nucleokinesis is characterized by two rapid polarity switches in the MTOC-to-nucleus axis.

Myosin-based forces drive amoeboid nucleokinesis to ensure adaptive pathfinding

When we measured the lengths of "losing" protrusions at path junctions, we observed that "losing" protrusion containing the nucleus were longer (Fig 4A and B) and required more time to retract (Fig 4A and C) compared to those without a nucleus, suggesting that retraction of protrusions containing the nucleus is a particular challenge (Fig 4D). This raised the question of which forces drive nuclear repositioning during amoeboid nucleokinesis. The positioning of the MTOC in front of the nucleus during the first phase of nucleokinesis suggested the possibility that microtubules emanating from the MTOC may couple to the nucleus, and thereby exert forces on the nucleus to pull it from the "losing" protrusion back to the cellular path. Yet surprisingly, when we depolymerized microtubules (Appendix Fig S4A–C), we did not observe any slowdown of amoeboid nucleokinesis (Figs 3F and EV3A–F, and Movie EV4). In contrary, nocodazole-treated cells showed, if at all, rather an accelerated speed of nucleokinesis (Fig EV3A and B) as well as repositioning frontward to the MTOC (Fig 3G and H). As microtubule depolymerization is known to cause increased cellular contractility by releasing microtubule-bound actomyosin regulators like the RhoA guanine nucleotide exchange factor GEF-H1/Lfc1 (Krendel et al, 2002; Bouchet & Akhmanova, 2017; Kopf et al, 2020), this finding raised the possibility that actomyosin contractility could be a driving force of amoeboid nucleokinesis. This notion was supported when we quantified the distance as well as the change of distance between the nucleus and the MTOC (Appendix Fig S3C–F), showing that the nucleus is even more distantly frontward positioned upon microtubule inhibition (Fig EV3E–G), as if the nucleus would be pushed to a frontward localization while the localization of the MTOC remains rather stable along the cell axis. Further, imaging of myosin-IIA localization during amoeboid nucleokinesis using MYH9-GFP encoding dendritic cells revealed an enriched myosin-IIA localization in retracting protrusions closely behind the nucleus (Fig 4E and F, and Movie EV5). Similarly, when we imaged the localization of actin (Lifeact-GFP) and myosin (MYH9-GFP) in the environments with one blocked path that allow the specific observations of nucleokinesis, we observed relocalisation of myosin from the previous cell rear toward the back of the nucleus-containing "losing" protrusion (Fig 4G), as if myosin forces would drive nucleokinesis.

To test whether myosin-IIA indeed provides forces to reposition the nucleus during amoeboid nucleokinesis, we next exposed motile DCs to the myosin-II inhibitor para-nitroblebbistatin (Képiró et al, 2014) (Fig EV4A and B). Cells with inhibited myosin failed to efficiently switch cell polarities during nucleokinesis, showing a random nucleus-to-MTOC axis configuration before, during, and after

nucleokinesis (Figs 4H and I, and EV4C–G, and Movie EV6). To corroborate these results, we analyzed myosin-IIA knockout DCs and also observed delayed reconfiguration of the nucleus-to-MTOC axis during amoeboid nucleokinesis (Appendix Fig S5A–D). Given the concerted action of myosin together with the actin cytoskeleton, we next inhibited the actin cytoskeleton with low-doses of latrunculin, which still enabled migration (Fig EV5A and B) but reduced the rate of cell polarity switching during nuclear repositioning (Figs 4J and EV5C–I). Thus, actomyosin contractility is required for efficient cell polarity switching during amoeboid nucleokinesis.

To test for the functional consequences of impaired amoeboid nucleokinesis, we next measured the speed of nucleokinesis and cellular path adaptions when myosin is nonfunctional. While the cellular speed before nucleokinesis was even mildly increased in the presence of the myosin-II inhibitor para-nitroblebbistatin (Fig EV4E), path adaptations in response to competing chemical and mechanical guidance cues occurred less rapidly (Fig 5A and B) and less frequently (Fig 5C). Notably, "losing" protrusions containing the nucleus were more affected by myosin inhibition than "losing" protrusions without a nucleus (Fig 5B), suggesting that myosin forces are not only required for protrusion retraction but are also particularly required when the protrusion contains a mispositioned nucleus. Similarly, when we analyzed path adaptions in environments completely independent of pore sizes, the repositioning of the nucleus from "dead"-end paths to the selected cellular paths was slowed down upon myosin (Figs 5D, E and G, and EV4D and E) and actin inhibition (Fig EV5E–G), causing a longer duration of nucleokinesis (Fig 5G) and even entire failure to adapt the nuclear to the cellular path, resulting in cells stuck in the wrong path (Fig 5H and Movie EV6). Quantification of the retraction time of "losing" protrusions with and without nucleus showed again that nucleus-containing protrusions are particularly susceptible for myosin inhibition (Fig 5E). To confirm these findings, we employed DCs with a knockout of the myosin regulator GEF-H1 (Lfc in mouse) and found a reduction in the retraction time of nucleus-containing "losing" protrusions, but not in the retraction time of "losing protrusions" without a nucleus and also not during migration in straight channels (Fig 5F and Appendix Fig S6A–F). Together, these findings identify actomyosin forces as a major driving factor of amoeboid nucleokinesis.

Adaptive pathfinding by nucleokinesis in the *Dictyostelium discoideum* amoebae

To explore whether adaptive pathfinding by amoeboid nucleokinesis is a general feature of amoeboid cell migration, we investigated motile single cells of the amoebae *Dictyostelium discoideum*. Comparable to immune cells, *Dictyostelium* cells typically explore their surrounding microenvironment with at least two protrusions (Andrew & Insall, 2007), until they select a path, followed by repeated cycles of protrusion formation, path exploration, and path selection (Fig 6A and Movie EV7). Using a nuclear marker during *Dictyostelium* pathfinding in an environmental maze along a chemotactic folate gradient, we discovered frequent nucleokinesis events from future "losing" into "winning" protrusions (Fig 6A and E), with rapid speeds faster than the cell front (Fig 6B) in the range of 8 to 25 μm/min (Fig 6C). Given the smaller cell body of *Dictyostelium* cells in comparison to DCs, the nucleokinesis distances of 10 μm

represented far-distant intracellular nuclear re-positioning throughout the cell body (Fig 6D). Thus, the basic parameters of nucleokinesis in *Dictyostelium* cells are highly comparable to nucleokinesis in immune cells (Fig 6C–E, and Appendix Fig S1A–C and Movie EV7). Next, to characterize the configuration of the nucleus-MTOC axis, we employed *Dictyostelium* cells encoding mRFP-histone as a marker for the nucleus and GFP-α-tubulin as a marker for the MTOC

(Fig 6F). Before a nucleokinesis event, *Dictyostelium* cells migrated in the typical amoeboid nucleus-forward configuration (Ishikawa-Ankerhold *et al*, 2022), but then switched to an MTOC-forward configuration during the first phase of nucleokinesis, followed by the restoration of the nucleus-forward configuration during the second phase (Fig 6F–H and Movie EV8). Notably, as in amoeboid immune cells, this two-step polarity switch is dependent on myosin-II
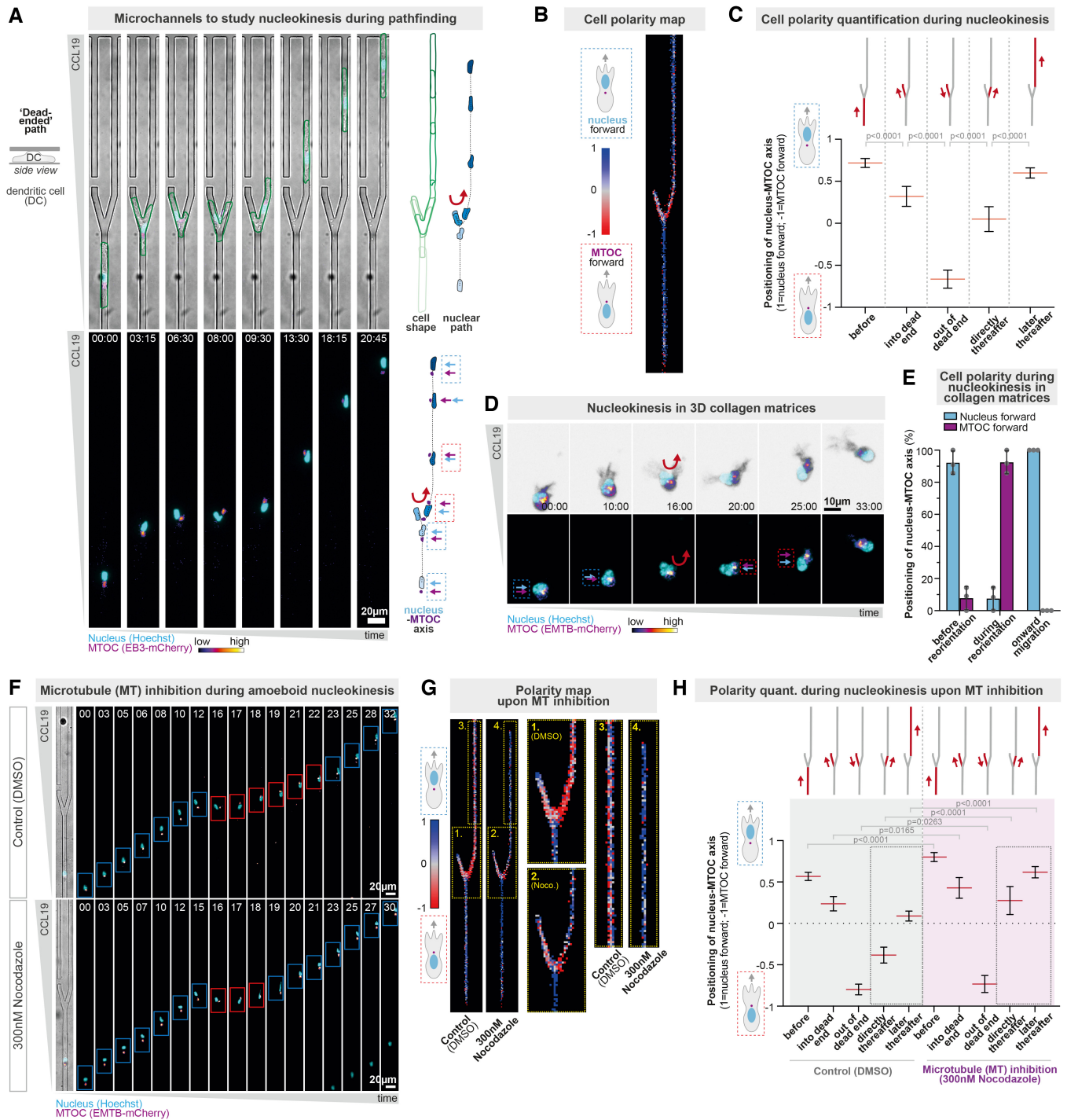

Figure 3.

◀

Figure 3. Two-step amoeboid nucleokinesis by consecutive cell polarity switches.

A   Representative Hoxb8-derived dendritic cell (DC) approaching a path decision with equal pore sizes but one blocked path, frequently causing nucleokinesis from the blocked to the open path. The DC stably encodes the microtubule plus-end marker EB3-mCherry, which also visualizes the microtubule-organizing center (MTOC; in pink). The nucleus is visualized by Hoechst (cyan) and the cell shape is outlined in green. Projections of cellular (green), MTOC (pink) and nuclear (blue) paths are shown on the right. The configuration of the nucleus-MTOC axis is highlighted by dashed boxes (blue = nucleus forward; red = MTOC forward). See also Fig EV1D–G for a detailed characterization of the assay. Time in min:s.

B   Heatmap of the nucleus-MTOC axis configuration during amoeboid nucleokinesis. The frontward positioning of the nucleus is depicted in blue and the frontward positioning of the MTOC is depicted in red. See also Fig EV1H for a more detailed description of the imaging quantification. $N = 6$ replicates, 48 cells.

C   Quantification of the nucleus-MTOC axis configuration before, during, directly after, and later after amoeboid nucleokinesis (1 = all cells position the nucleus in front of the MTOC; −1 = all cells position the MTOC in front of the nucleus). Data are mean ± 95CI, Mann–Whitney test, $N = 6$ replicates, 48 cells, and 660 (before), 250 (into a dead end), 191 (out of a dead end), 179 (directly thereafter), and 678 (later thereafter) image frames.

D   Representative HoxB8-derived DCs stably encoding EMTB-mCherry (visualizes the MTOC; fire-color coded) and transiently stained with Hoechst (visualizes the nucleus; cyan), migrating in a three-dimensional collagen network along a CCL19 chemokine gradient. The cell shape is shown in black (via high intensity of the EMTB-mCherry channel). Note the nucleokinesis event from the left protrusion into the right protrusion. Time in min:s.

E   Quantification of the nucleus-MTOC axis configuration of DCs (stably encoding EB3-mCherry to viualize the MTOC) migrating in 3D collagen networks and performing nucleokinesis. The nucleus-MTOC axis configuration was analyzed before, during, and after the nucleokinesis event. Data are mean ± SD. $N = 3$ replicates, 32 cells.

F   Representative HoxB8-derived DCs in the presence of the microtubule inhibitor nocodazole (300 nM) or control (DMSO). The DCs stably encode EMTB-mCherry (to visualize the MTOC; fire-color coded) and is transiently stained with Hoechst (to visualize the nucleus; cyan). The configuration of the nucleus-MTOC axis is highlighted by boxes (blue = nucleus forward; red = MTOC forward). Time in min.

G   Heatmap of the nucleus-MTOC axis configuration during amoeboid nucleokinesis in the presence of the microtubule inhibitor nocodazole (300 nM) or control (DMSO). The yellow-dotted regions 1 (DMSO) and 2 (Nocodazole) are enlarged to depict the cellular behavior during the initial nucleokinesis event, and the yellow-dotted regions 3 (DMSO) and 4 (Nocodazole) are enlarged to depict the cellular behavior during the later nucleokinesis events to reposition the nucleus to the cellular front. $N = 3$ replicates, 96 (DMSO) and 36 (Nocodazole) cells.

H   Quantification of the nucleus-MTOC axis configuration before, during, directly after, and later after amoeboid nucleokinesis in the presence of the microtubule inhibitor nocodazole (300 nM) or control (DMSO) (1 = all cells position the nucleus in front of the MTOC; −1 = all cells position the MTOC in front of the nucleus). Data are mean ± 95CI, Mann–Whitney test, $N = 3$ replicates, 96 (DMSO) and 36 (Nocodazole) cells, and 1,096 (before; DMSO), 463 (before; nocodazole), 493 (into a dead end, DMSO), 203 (into a dead end, nocodazole), 338 (out of a dead end, DMSO), 172 (out of a dead end, nocodazole), 360 (directly thereafter, DMSO), 127 (directly thereafter, nocodazole), 1,062 (later thereafter, DMSO), and 508 (later thereafter, nocodazole) image frames.

Source data are available online for this figure.

contractility, as the positioning of the nucleus to the front of the cell axis was strongly delayed in the presence of the myosin-II inhibitor para-nitroblebbistatin (Fig 6I, and Appendix Fig S7A and B, and Movie EV9). To corroborate these results, we analyzed *Dictyostelium* cells bearing a well-established myosin-II null mutation (myosin-II deficient (mhcA-null) strain HS2205) (Manstein *et al*, 1989; Bindl *et al*, 2020), as well as genetically encoded markers for the nucleus and the MTOC (mRFP-histone and GFP-α-tubulin), and also observed delayed nuclear relocalization frontward to the MTOC during nucleokinesis (Fig 6J and K, and Movie EV9). Thus, despite the phylogenetic distance between mammalian immune cells and the amoebae *D. discoideum*, the mechanistic principles of amoeboid nucleokinesis during cellular navigation are conserved.

Together, these findings identify amoeboid nucleokinesis as a conserved process in rapid amoeboid migrating cells, comprising a two-step cell polarity switch driven by myosin-II forces, sliding the nucleus from a "losing" to the "winning" protrusion to ensure adaptive pathfinding in complex microenvironments.

Discussion

Cellular organelles are often actively positioned to defined subcellular locations within the cytoplasm (Bornens, 2008). This active positioning includes membrane-surrounded organelles like the nucleus and mitochondria, but also membraneless-organelles like the microtubule-organizing center (MTOC). The active positioning of the genome-carrying nucleus is particularly challenging (Gundersen & Worman, 2013), as it is typically the largest and stiffest organelle (Kalukula *et al*, 2022). Cells solved this challenge by exerting forces

from the cytoskeleton onto the nucleus, leading to its intracellular movement and positioning—a process referred to as nucleokinesis, by which the entire nucleus moves intracellularly in relation to the cell's shape. For instance, cells in the developing vertebrate neuroepithelium employ forces that are mainly generated by the actomyosin cytoskeleton to move their nuclei basally and apically during the progression of the cell cycle (Norden *et al*, 2009), whereas the movements of female and male pronuclei during fertilization are mainly driven by forces from the microtubule cytoskeleton (Reinsch & Gonczy, 1998).

An additional complexity for nuclear positioning arises when cells are not stationary but motile (Calero-Cuenca *et al*, 2018), adding the challenge of coordinating nuclear positioning with the cellular advance along the migratory path. Key findings showed that motile fibroblasts reposition their nucleus to the cellular rear to start their movement into cell-free tissue wounds (Luxton *et al*, 2010; Zhu *et al*, 2018). Mechanistically, this rearward nuclear positioning is driven by an actin cortex composed of actin cables that are coupled to the nucleus and move against the direction of cellular movement (Luxton *et al*, 2010). Fibroblasts are mesenchymally migrating cells that adhere to their extracellular environments and migrate with velocities in the range of tens of micrometers per hour. Thus, the principles and mechanisms of nuclear positioning in stationary and slowly moving cells are increasingly well understood. However, how extremely fast migrating cells coordinate the intracellular positioning of the nucleus with their migration path remained entirely unknown. The high velocities of fast migrating cells, which are typically around 10 μm/min, even raised the question of whether nuclear movement can be at all faster than the cellular speed—a prerequisite for active nuclear repositioning in relation to the movement of the cell body.
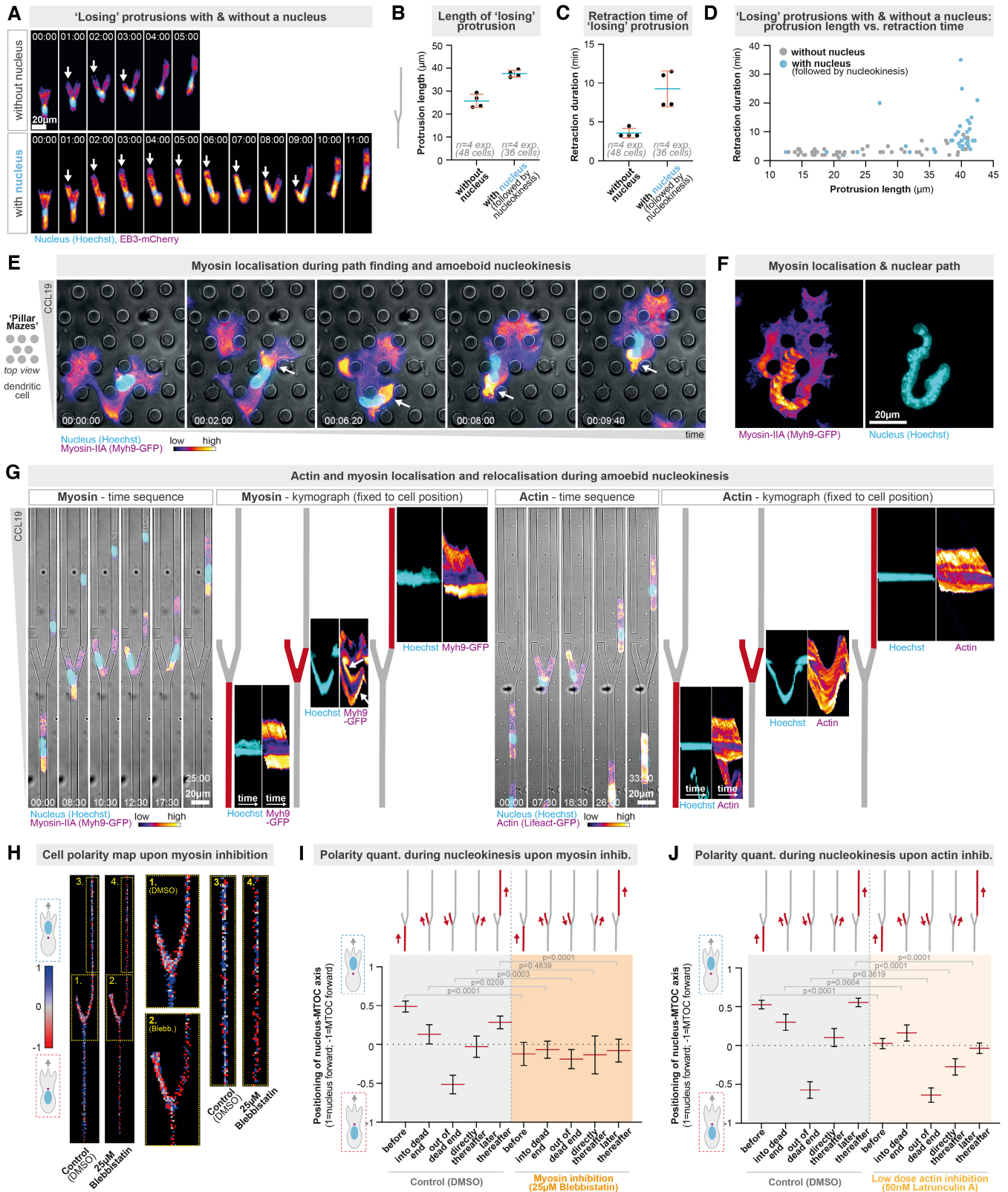
Figure 4.

◀ **Figure 4. Cell polarity switches during amoeboid nucleokinesis require a functional actomyosin cytoskeleton.**

A   Protrusion lengths of representative EB3-mCherry encoding DCs approaching a path decision with equal pore sizes but one blocked path, either with or without nucleus in the "losing" protrusion. The nucleus (Hoechst) is shown in cyan. Time in min:s.

B   Quantification of the lengths of "losing" protrusions, comparing 'losing' protrusions without a nucleus and with a nucleus. Data are Mean ± SD. N = 4 replicates (48 cells and 36 cells). Note that "losing" protrusions with a nucleus are longer than "losing" protrusions without a nucleus. See also (D) for a direct comparison of the retraction time of long "losing" protrusions with and without a nucleus.

C   Quantification of the retraction time of "losing" protrusions, comparing "losing" protrusions without a nucleus and with a nucleus. Data are Mean ± SD. N = 4 replicates (48 and 36 cells).

D   Protrusion length vs. retraction time. N = 4 replicates.

E   Representative HoxB8-derived Myh9-GFP expressing DC migrating through a porous maze-like microenvironment composed of pillars interconnecting two surfaces below and above the migrating cell. Myh9-GFP localization is fire color-coded and the nuclear localization is shown in cyan (transient Hoechst label). Time in h:min:s.

F   Time projection of Myh9-GFP and nuclear localization of the cell shown in (E).

G   Representative HoxB8-derived Myh9-GFP (left) and Lifeact-GFP (right) expressing DCs migrating through a path decision junction with equal pore sizes but one blocked path. The Myh9-GFP and Lifeact-GFP signal is fire color-coded and the nuclear localization is shown in cyan (transient Hoechst label). The kymographs show the signals over time and are depicted by fixing the position of the cell (see Materials and Methods for details) to better compare the signal distribution over time. Note the re-localization of the major Myh9-GFP signal from the back of the cell towards the back of the "losing" protrusion during nucleokinesis (white arrows).

H   Heatmap of the nucleus-MTOC axis configuration during amoeboid nucleokinesis in the presence of the myosin-II inhibitor para-nitroblebbistatin (25 μM) or control (DMSO). The yellow-dotted regions 1 (DMSO) and 2 (para-nitroblebbistatin) are enlarged to depict the cellular behavior during the initial nucleokinesis event, and the yellow-dotted regions 3 (DMSO) and 4 (para-nitroblebbistatin) are enlarged to depict the cellular behavior during the later nucleokinesis events to reposition the nucleus to the cellular front. N = 4 replicates, 37 (DMSO) and 13 (para-nitroblebbistatin) cells.

I   Quantification of the nucleus-MTOC axis configuration before, during, directly after, and later after amoeboid nucleokinesis in the presence of the myosin-II inhibitor para-nitroblebbistatin (25 μM) or control (DMSO) (1 = all cells position the nucleus in front of the MTOC; −1 = all cells position the MTOC in front of the nucleus). Data are mean ± 95CI, Mann–Whitney test, N = 4 replicates, 37 (DMSO) and 13 (para-nitroblebbistatin) cells, and 582 (before; DMSO), 173 (before; para-nitroblebbistatin), 246 (into a dead end, DMSO), 315 (into a dead end, para-nitroblebbistatin), 198 (out of a dead end, DMSO), 244 (out of a dead end, para-nitroblebbistatin), 208 (directly thereafter, DMSO), 67 (directly thereafter, para-nitroblebbistatin), 523 (later thereafter, DMSO), and 180 (later thereafter, para-nitroblebbistatin) image frames.

J   Quantification of the nucleus-MTOC axis configuration before, during, directly after, and later after amoeboid nucleokinesis in the presence of the actin inhibitor LatrunculinA (50 nM) or control (DMSO) (1 = all cells position the nucleus in front of the MTOC; −1 = all cells position the MTOC in front of the nucleus). Data are mean ± 95CI, Mann–Whitney test, N = 3 replicates, 78 (DMSO) and 13 (LatrunculinA) cells, and 900 (before; DMSO), 866 (before; LatrunculinA), 323 (into a dead end, DMSO), 351 (into a dead end, LatrunculinA), 234 (out of a dead end, DMSO), 265 (out of a dead end, LatrunculinA), 281 (directly thereafter, DMSO), 328 (directly thereaf-ter, LatrunculinA), 902 (later thereafter, DMSO), and 899 (later thereafter, LatrunculinA) image frames.

Source data are available online for this figure.

On top of this speed challenge, rapidly migrating cells also provide a morphological challenge: the fastest migrating cells are typically amoeboid cells, including many immune cells, which have complex, ramified cell shapes that dynamically and constantly change during navigation along the migration path, raising the question whether and how nuclear positioning is coordinated with these highly dynamic changes in cell shape.

Here, we investigated major cellular models of fast amoeboid migrating cells, including immune cells (dendritic cells and T cells) and the single-cell amoeba *D. discoideum*, and discovered that motile amoeboid cells actively move and reposition their nuclei during pathfinding. Nuclear movement in amoeboid cells is extraordinarily efficient and frequent, functioning in a very rapid manner over long intracellular distances. Given the similarity of this type of nuclear movement to the movement properties of entire amoeboid cells, we name this newly described mode of nuclear movement as "amoeboid nucleokinesis." Amoeboid nucleokinesis appears to function independently of a direct role of the microtubule cytoskeleton, as microtubule depolymerization did not impair the speed of nuclear repositioning. Instead, our findings show that amoeboid nucleokinesis requires forces from the actomyosin cytoskeleton. While forces from actin and myosin are well known to be important for the advance and retraction of individual protrusions and the entire cell body, as well as for the squeezing of the cell body and the nucleus (Lämmermann *et al*, 2008; Thiam *et al*, 2016; Barbier *et al*, 2019), our reductionistic microchannel approach enabled us to investigate the principles of amoeboid nucleokinesis independent of squeezing and general migration or retraction defects. This approach revealed

that the retraction of a "losing" protrusion containing the nucleus is a particular challenge, requiring myosin forces to reposition the nucleus towards the "winning" protrusion during the first phase of nucleokinesis and into an intracellular location ahead of the MTOC during the second phase. Given the rapid temporal scale of nuclear repositioning and the two rapid switches in the nucleus-MTOC axis configuration, it will be interesting to investigate whether amoeboid nucleokinesis may involve a tight anchorage between the actomyosin cytoskeleton and the nucleus, or may function through an anchorage-independent mechanism driven by myosin forces located at the rear of the nucleus. Considering the accumulation of myosin behind the nucleus, it is tempting to speculate that myosin pushes the nucleus during amoeboid nucleokinesis. Alternatively, myosin may also pull the nucleus from the front, which though would likely require tight anchorage between actomyosin filaments and the nucleus, and adhesive cellular contacts with the microenvironment to stably attach the pulling force, the latter being less typical for non- or low-adhesive amoeboid migrating cells.

Functionally, we discover that amoeboid nucleokinesis is required for amoeboid cell migration in complex mechanochemical microenvironments. Specifically, amoeboid nucleokinesis allows cells to adapt their path flexibly when a dominant guidance cue emerges, in particular when the nucleus follows initially the path of least resistance through a larger pore but then the cell decides to migrate along the path of another, alternative protrusion along a dominating chemotactic cue. When amoeboid nucleokinesis is impaired, cells are less efficient to adapt their path and may become trapped. Tissue microenvironments typically present a variety of

chemical and mechanical cues, including differently sized pores. These microenvironmental pores can be very heterogenous in size, typically in the range of 2–10 µm, and are thus considerably

smaller than the cellular diameter (Wolf *et al*, 2009; Weigelin *et al*, 2012; Kameritsch & Renkawitz, 2020). While motile amoeboid cells can use their nucleus as a gauge to probe for the pore
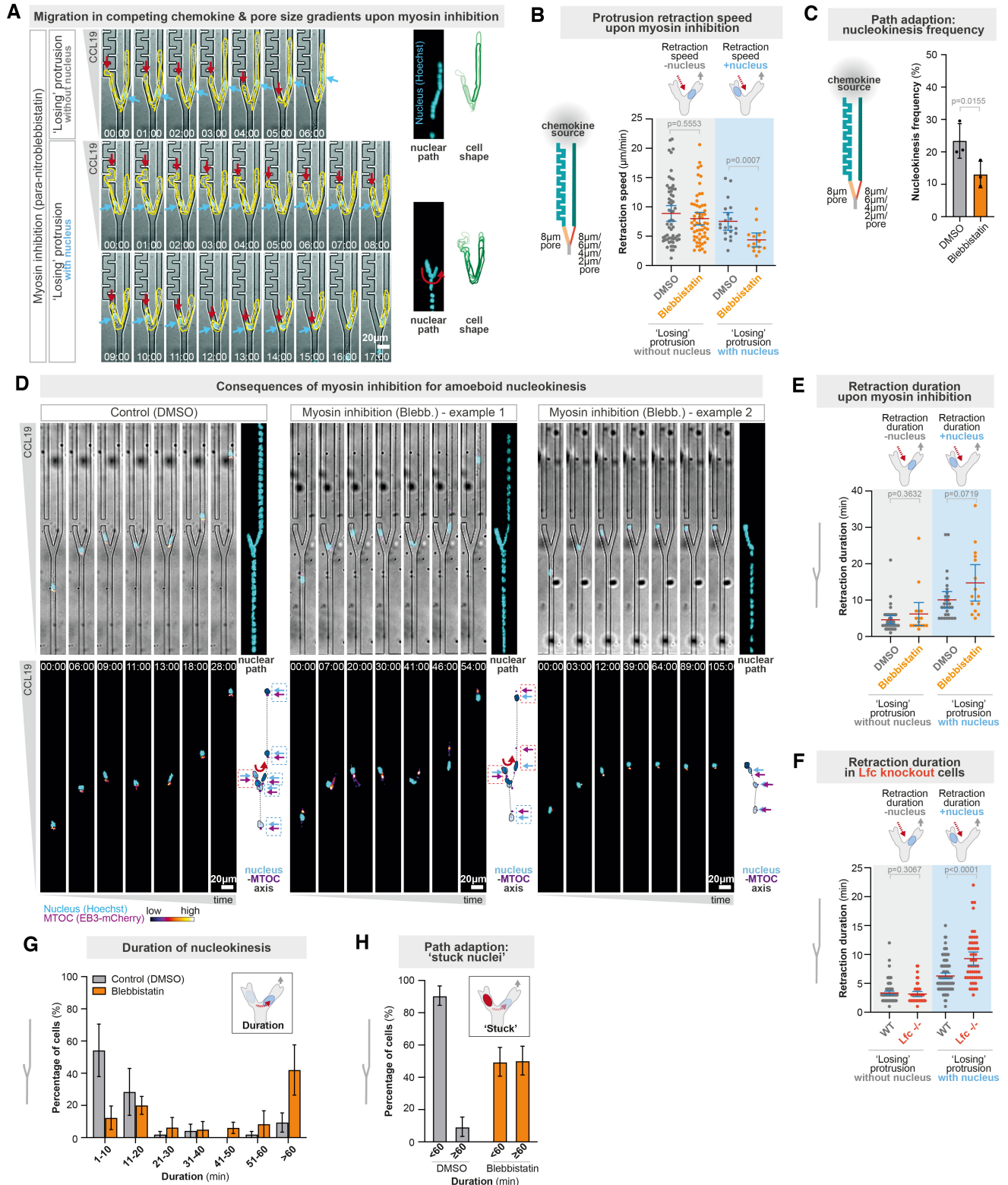

Figure 5.

Figure 5. Myosin-based forces drive amoeboid nucleokinesis to ensure adaptive pathfinding.

A Representative bone-marrow derived DCs migrating through path decision with competing chemokine and pore size gradients in the presence of the myosin-II inhibitor para-nitroblebbistatin (25 μM), showing representative cells with and without the nucleus in the 'losing' protrusion. The cell shape is outlined in yellow, and the red arrow highlights the retraction of the "losing" protrusion. The nucleus is shown in cyan (Hoechst) and highlighted by cyan arrows.

B Quantification of (A), measuring the retracting speed of "losing" protrusions in the presence of the myosin-II inhibitor para-nitroblebbistatin (25 μM) or control (DMSO), depending on whether the "losing" protrusion contains the nucleus or not. Data are Mean ± 95CI, Mann–Whitney test, $N = 3$ replicates, 61 (DMSO, without nucleus), 59 (para-nitroblebbistatin, without nucleus), 20 (DMSO, with nucleus), and 15 (para-nitroblebbistatin, with nucleus) cells.

C Quantification of (A), measuring the frequency of how often the cell adapts its path by nuclear reorientation from a "losing" towards a "winning protrusions in the microenvironments described in Fig 2. Data are Mean ± SD, paired t test, $N = 3$ replicates, 182 (DMSO), and 136 (para-nitroblebbistatin) cells.

D Representative HoxB8-derived DCs in the presence of the myosin-II inhibitor para-nitroblebbistatin (25 μM) or control (DMSO). The DCs stably encode EB3-mCherry (to visualize the MTOC; fire color-coded) and are transiently stained with Hoechst (to visualize the nucleus; cyan). The left panel shows a representative control cell, the middle panel a representative myosin-inhibited cell with delayed nuclear repositioning to the front of the cell, and the right panel a representative myosin-inhibited cell that entirely fails to reposition to the productive open path. The configuration of the nucleus-MTOC axis is highlighted by dashed boxes (blue = nucleus forward; red = MTOC forward). Time in min:s.

E Quantification of the retracting speed of "losing" protrusions in the presence of the myosin-II inhibitor para-nitroblebbistatin (25 μM) or control (DMSO), depending on whether the "losing" protrusion contains the nucleus or not. Data are Mean ± 95CI, Mann–Whitney test, $N = 4$ replicates, 60 (DMSO) and 25 (para-nitroblebbistatin) cells.

F Quantification of the retracting speed of "losing" protrusions in control (WT) or Lfc$^{-/-}$ DCs, depending on whether the "losing" protrusion contains the nucleus or not. Data are Mean ± 95CI, Mann–Whitney test, $N = 4$ replicates, 226 (WT) and 104 (Lfc$^{-/-}$) cells.

G Quantification of the duration of nucleokinesis in the presence of the myosin-II inhibitor para-nitroblebbistatin (25 μM) or control (DMSO). Data are mean ± SEM. $N = 3$ replicates, 50 (DMSO) and 38 (para-nitroblebbistatin) cells.

H Quantification of the percentage of cells that have a nucleus stuck in the blocked path for at least 60 min (myosin-II inhibitor para-nitroblebbistatin (25 μM) vs. control (DMSO)). Data are mean ± SEM. $N = 3$ replicates, 50 (DMSO) and 38 (para-nitroblebbistatin) cells.

Source data are available online for this figure.

size to select migration routes along larger, less detrimental pores (Renkawitz *et al*, 2019), cells should be able to flexibly redirect their migration path upon the emergence of other cues. Here we showed this flexibility in microenvironments of competing chemokine and pores size cues, identifying that high chemokine concentrations can overrule pore size cues. Such a behavior appears to be highly relevant in physiological situations when cells are directed by chemotactic cues into dense or narrow tissue microenvironments, such as when mature dendritic cells have to squeeze themselves through tiny openings of lymph capillaries during their travel to the lymph node (Pflicke & Sixt, 2009). Considering that virtually all motile cells simultaneously encounter a variety of chemical and mechanical signals in their immediate local microenvironment, our findings suggest that nucleokinesis plays a universally crucial role in the navigation of migrating cells.

Figure 6. Adaptive pathfinding by nucleokinesis in *Dictyostelium discoideum* amoebae.

A Representative *Dictyostelium discoideum* cell migrating through a porous maze-like microenvironment composed of pillars interconnecting two surfaces below and above the migrating cell. The *Dictyostelium* cell stably expresses mRFP-histone (to visualize the nucleus; cyan) and the cell shape is outlined in green. Time projections of the cellular and nuclear paths are shown in shades of green and blue, respectively. Time in h:min:s.

B Quantification of the speed of nuclear and cell front movement during nucleokinesis in *Dictyostelium* cells. Independent speeds of nucleus and cell front are shown on the left. Nuclear speed normalized to the cell front speed (fold change) is shown on the right. Data are mean ± SD. $N = 3$ replicates, 25 cells.

C Quantification of the speed of nuclear movement during nucleokinesis in DCs and *Dictyostelium* cells migrating in pillar mazes (DCs in pillars mazes with 9 μm pores sizes, and *Dictyostelium* cells in pillar mazes with 5 μm pore sizes). Data are median ± 95CI. $N = 3$ replicates, 25 (*Dictyostelium*) and 30 (DCs) cells.

D Quantification of the intracellular distance of nuclear movement during nucleokinesis in DCs and *Dictyostelium* cells migrating in pillar mazes. Data are median ± 95CI. $N = 3$ replicates, 25 (*Dictyostelium*) and 30 (DCs) cells.

E Quantification of the rate (left) and frequency (right) of nucleokinesis events in amoeboid migrating *Dictyostelium* cells and DCs. Rate: when the migrating cell has a least two major protrusions, quantification of whether the nucleus locates immediately into the dominant protrusion or first locates into the future retracting protrusion, requiring nucleokinesis into the future dominant protrusion. Frequency: showing the frequency of at least two leading edges and nucleokinesis events per minute. Data are mean ± SD. $N = 3$ replicates, 25 (*Dictyostelium*) and 30 (DCs) cells.

F Representative *Dictyostelium* cell migrating in a pillar maze. The *Dictyostelium* cell stably encodes GFP-α-tubulin, which also visualizes the microtubule-organizing center (MTOC; in pink) and mRFP-histone, which visualizes the nucleus (in cyan). The cell shape is outlined in green. Projections of cellular (green), MTOC (pink) and nuclear (blue) paths are shown on the right. Red arrows highlight full and partial nucleokinesis events. Time in min:s.

G Quantification of the nucleus-MTOC axis configuration before and during nucleokinesis. Data are mean ± SD. $N = 3$ replicates, 25 cells.

H Quantification of the nucleus-MTOC axis configuration after nucleokinesis. The x-axis indicates the number of pillar crossings after nucleokinesis. Data are mean ± SD. $N = 3$ replicates, 25 cells.

I Quantification of the nucleus-MTOC axis configuration before, during, and after nucleokinesis upon myosin inhibition. Data are mean ± SD. $N = 3$ replicates, 30 (DMSO) and 27 (para-nitroblebbistatin) cells.

J Representative *Dictyostelium* cells (WT: top, HS2205 myosin mutant: bottom) migrating in a pillar maze. The *Dictyostelium* cells stably encode GFP-α-tubulin, which also visualizes the microtubule-organizing center (MTOC; in pink) and mRFP-histone, which visualizes the nucleus (in cyan). The cell shape is outlined in green. Projections of cellular (green), MTOC (pink) and nuclear (blue) paths are shown on the right. Red arrows highlight full and partial nucleokinesis events. Time in min:s.

K Quantification of the nucleus-MTOC axis configuration before, during, and after nucleokinesis upon myosin mutation. Data are mean ± SD. $N = 3$ replicates, 25 (WT) and 26 (HS2205; myosin mutant) cells.
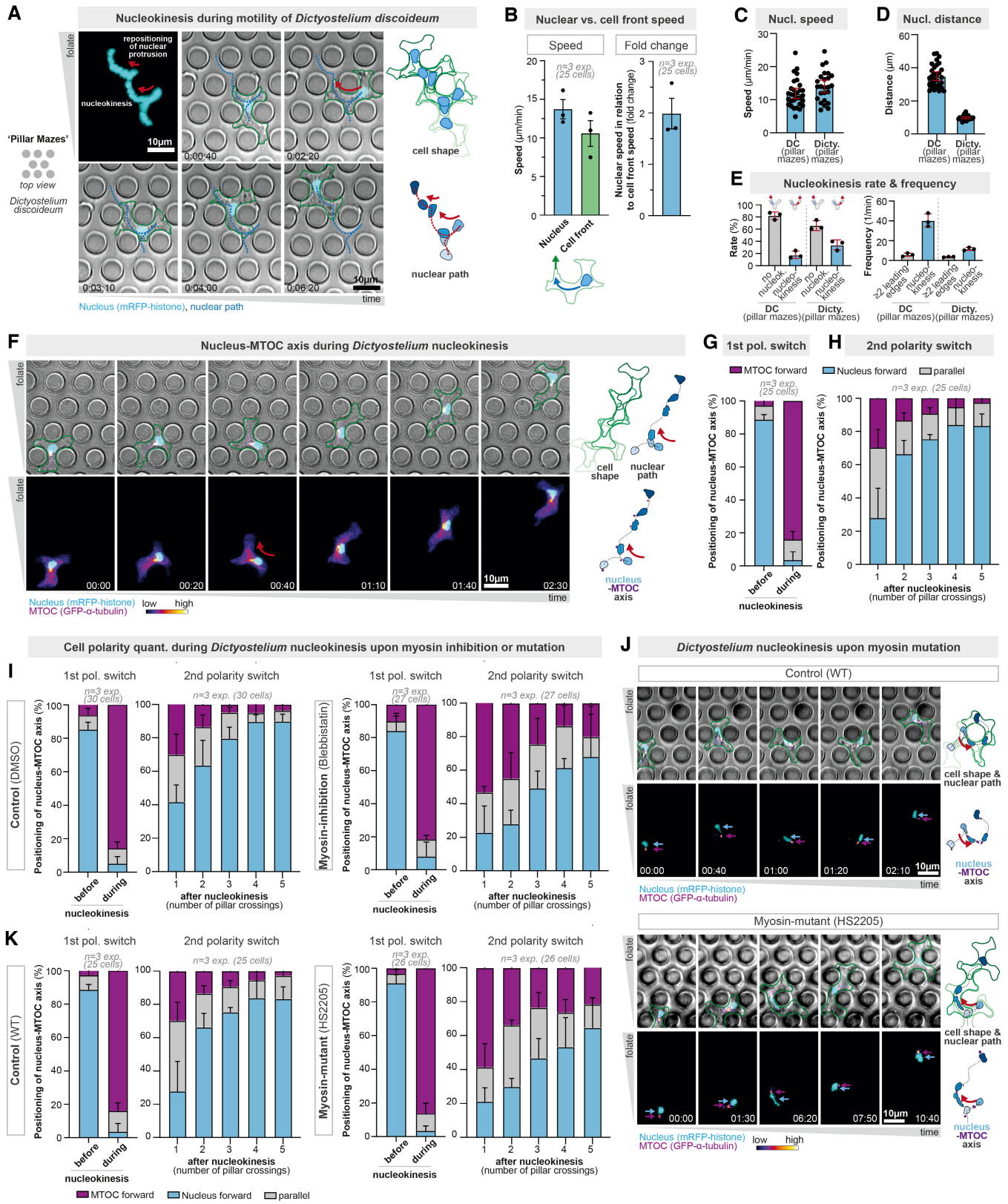
Source data are available online for this figure.

Figure 6.

Materials and Methods

Cell culture

Mammalian cell culture

All cells were kept at 37°C in a humidified incubator with 5% CO_2. DCs were differentiated either from the bone marrow of male C57B16/J wildtype mice (aged 8–12 weeks), male or female MyoIIA-Flox*CD11c-Cre mice (aged 8–11 weeks), or from Hoxb8 precursor lines (EB3-mCherry, EMTB-mCherry, Lifeact-GFP, Myh9-GFP, $Lfc^{+/+}$ (WT control) and $Lfc^{-/-}$ (KO)). Cells were differentiated in R10 medium (RPMI 1640 supplemented with 10% fetal calf serum (FCS), 2 mM L-glutamine, 100 U/ml penicillin, 100 mg/ml streptomycin, and 0.1 mM 2-mercaptoethanol; all Gibco) supplemented with 10% granulocyte-macrophage colony-stimulating factor (GM-CSF) hybridoma supernatant. Fresh medium was added on differentiation days 3 and 6. To induce maturation, either fresh or thawed DCs (differentiation day 8) were stimulated for 24 h with 200 ng/ml lipopolysaccharide (LPS; *E. coli* O26:B6, Sigma-Aldrich) and used for experiments on day 9. DCs derived from bone marrow from MyoIIA-Flox*CD11c-Cre mice were additionally differentiated for two more days (to enable longer Cre expression under the control of CD11c): additional fresh medium was added at day 8 and the cells were frozen at day 10, followed by stimulation with LPS upon thawing, and usage of the cells for experiments on day 11.

T cells were isolated from the spleen of male or female C57BL/6J mice (aged 6–12 weeks) using the EasySep mouse naive T cell isolation Kit (Stemcell). Cells were seeded onto cell culture plates coated with 1 μg/ml CD3 antibody and 1 μg/ml CD28 antibody and either used for experiments between differentiation days 3 and 6 or frozen at day 6 and thawed for experiments.

Dictyostelium discoideum

Cells of the *D. discoideum* strain AX2-214 (here designated as wild type), and the myosin-II deficient (mhcA-null) strain HS2205 derived from it (Manstein *et al*, 1989) were used. Nuclei and microtubules in both strains were visualized by expression of GFP-α-tubulin (tubA1; DDB0191380|DDB_G0287689) and mRFP-histone (H2Bv3; DDB0231622|DDB_G0286509) (Bindl *et al*, 2020; Ishikawa-Ankerhold *et al*, 2022). Cells were cultured in polystyrene Petri dishes containing HL5 medium (Formedium, Hunstanton, Norfolk, UK) supplemented with 10 μg/ml of blasticidin S (Gibco, Fisher Scientific GmbH, Schwerte, Germany), 20 μg/ml of geneticin (Sigma-Aldrich, Sigma-Aldrich Chemie GmbH, Taufkirchen, Germany), or 33 μg/ml hygromycin B (EMD Millipore Corp., Billerica, MA, USA) at 22°C. While the myosin-II-deficient mutant has been reported to have cytokinesis defects causing multinucleation, our adhesive cell culture conditions mostly resulted in single-nucleated cells and for analysis we only included those single-nucleated cells.

Mice

Wild-type animals were housed in the Core Facility Animal Models at the Biomedical Centre (Ludwig-Maximilians-Universität), and animal procedures and experiments were in accordance with the ministry of animal welfare of the region of Oberbayern and with the German law of animal welfare.

Flow cytometry analysis

DCs were routinely checked for surface marker expression using antibodies for CD11c (17-0114-82, Invitrogen) and MHCII (48-5321-82, Invitrogen). After Fc receptor blockage using an antibody for CD16/32 (14-0161-85, Invitrogen), stainings were performed in FACS buffer (1% BSA, 2 mM EDTA in PBS). Cells were analyzed using a Cytoflex S flow cytometer (Beckmann-Coulter).

Microfabricated devices

Microfabricated devices were generated as described previously (Renkawitz *et al*, 2018; Kroll *et al*, 2022). In brief, wafers produced by photolithography or epoxy replicates thereof were used as templates for micro-structures with defined lengths, widths, and heights. Microchannels had a width of 8 μm. For analysis of adaptive pathfinding in competing chemokine and pore-size cues, pores were 2, 4, or 6 μm wide. Pore sizes in pillar forests were 5 and 9 μm for *D. discoideum* and DC migration, respectively. The height of the micro-structures ranged from 4 to 5 μm to ensure cell confinement from all sides.

Polydimethylsiloxane (PDMS; 10:1 mixture of Sylgard 184, Dow) was cast on the template micro-structures. PDMS was mixed in a Thinky mixer, and air bubbles were removed in a desiccator. After curing at 80°C overnight, PDMS was removed from the template and cut into single devices. Holes were punched on each side of the micro-structures to enable cell and chemokine loading. Subsequently, PDMS pieces were bonded to cleaned coverslips using a plasma cleaner. PDMS devices were placed at 120°C for 10 min and at 80°C overnight to ensure permanent bonding.

Simulation of chemokine diffusion

The geometry of an exemplary channel of the microchannel design was traced from a transmitted light image in Fiji and subsequently exported. A 2D model of the channel was generated from this data, and time-dependent diffusion was simulated using MATLAB's "solvepde" function. The boundary condition at the channel interface with the chemokine source was set to c_0, and at the interface with the drain, it was set to 0 (Dirichlet boundary conditions). We used a diffusion constant of 1.3e-10 m^2/s for CCL19, as previously described (Schwarz *et al*, 2016).

Live-cell migration assays

To visualize the nucleus for live-cell migration assays, cells were incubated with 1 drop of NucBlue (Invitrogen) in 1 ml of cell/media mixture for at least 30 min. SPY555-tubulin (Spirochrome) was used according to the manufacturer's protocol to visualize the MTOC. For pharmacological inhibition experiments, cells were treated with final concentrations of 50 nM Latrunculin A (Sigma-Aldrich), 25 μM para-nitroblebbistatin (Motorpharma; dissolved in DMSO), or 300 nM or 10 μM Nocodazole (Sigma-Aldrich). Control samples were treated with the respective DMSO dilution.

Microchannel migration assays

PDMS devices were flushed with phenol-free R10 medium supplemented with 50 μM L-ascorbic acid (Sigma-Aldrich) and pharmacological inhibitors if applicable for the experimental setup. Devices were

incubated at 37°C, 5% CO$_2$ for at least 1 h before the experiment. Subsequently, 0.625 μg/ml CCL19 (DCs) or 100 μM folate (*Dictyostelium*) were loaded into the chemokine loading hole to establish a gradient. Finally, 0.1–1 × 10^5 cells were added into the opposite loading hole. When performing experiments with *Dictyostelium* cells in microchannels using either folate or cAMP as chemotactic cue, we rarely observed cells reaching the path decision points, as the microchannel designs included a long straight path before the path decision point. Thus, when investigating nucleokinesis in *Dictyostelium* cells, we loaded *Dictyostelium* into pillar forests, in which the cells immediately encounter a microenvironment with alternative path options on their migration path, enabling the investigation of nucleokinesis.

Visualization of chemokine gradient

For indirect visualization of the CCL19 gradient in the microchannels with competing chemokine and pore size gradients, 200 μg/ml dextran (10 kDa) coupled to Alexa Fluor™ 647 (Invitrogen) with a molecular weight and hydrodynamic radius comparable to CCL19 (Schwarz *et al*, 2016; Frick *et al*, 2018) was added to the chemokine loading hole.

Collagen migration assays

Collagen migration assays were performed as described previously (Kroll *et al*, 2022). Briefly, for DC or T cell migration in collagen, 1× minimum essential medium (MEM, Gibco), 0.4% sodium biocarbonate (Sigma-Aldrich), and Nutragen bovine collagen (Advanced BioMatrix) were mixed with 3–5 × 10^5 cells in R10 medium at a 2:1 ratio, resulting in a final collagen density of 3.3 mg/ml. The collagen-cell solution was added into custom-made migration chambers (appr. 17 mm in width and 1 mm in height). After 75 min polymerization at 37°C, 5% CO$_2$, gels were overlaid with 80 μl CCL19 (0.625 μg/ml). For pharmacological inhibition experiments, inhibitors were added to the chemokine solution as well as the collagen-cell solution.

Under-agarose migration assays

Under-agarose migration assays were performed as described previously (Clausen *et al*, 2022). In brief, 4% UltraPure agarose (Invitrogen) in sterile water was mixed with 55°C prewarmed phenol-free RPMI-1640 (Gibco) supplemented with 20% FCS and 1× Hanks buffered salt solution pH 7.3 in a 1:3 ratio resulting in a final agarose concentration of 1%. The 1% agarose mixture was allowed to cool to 37°C before introducing the inhibitor to the respective final concentration. 300 μl of the agarose mixture were poured into each well of imaging-suitable 8-well slides (Ibidi). The under-agarose migration assay was left at room temperature for 1 h to polymerize and was subsequently transferred to an incubator (37°C, 5% CO$_2$) for another hour to equilibrate. After equilibration, four 2 mm holes were punched in each well using tissue biopsy punchers. 2.5 μg/ml CCL19 in phenol-free R10 were loaded into two adjacent loading holes. Finally, 1.5 × 10^5 cells were loaded into each of the two opposite loading holes. The under-agarose migration assay was placed in the incubator for 4–5 h to let cells migrate under the agarose layer toward the chemokine source.

Immunofluorescence stainings

For immunofluorescence stainings, under-agarose migration assays were prepared as described above. Subsequently, cells were fixed by adding prewarmed 3.7% paraformaldehyde (PFA, diluted in PBS) on top of the agarose. After 1 h of fixation at 37°C, 5% CO$_2$, PFA, and the agarose block were carefully removed, and cells were washed 3 times with PBS. Permeabilization was conducted with 1× SAPO buffer (0.2% BSA + 0.05% saponin diluted in PBS) for 30 min, followed by blocking with 5% BSA (diluted in 1× SAPO) for another 30 min. Primary antibodies were incubated at 4°C overnight (rat anti-α-tubulin: 1 μg/ml, MA1-80017, Invitrogen; diluted in 1× SAPO). Following washing of the cells with PBS (3 times), samples were stained with secondary antibodies (goat anti-rat Alexa Fluor™ Plus 647: 4 μg/ml, A48265, Invitrogen; diluted in 1× SAPO) and DAPI (1:1,000, Thermo Fisher Scientific) at room temperature for 1 h. Following washing with PBS (3 times), samples were mounted using Fluoromount-G (Invitrogen).

Imaging

Live-cell imaging of dendritic cells and T cells was performed at 37°C and with 5% CO$_2$ in a humidified chamber. Live-cell imaging of *D. discoideum* was conducted at room temperature (22°C). Data were recorded using inverted DMi8 microscopes (Leica) with HC PL FLUOTAR 4×/0.5 PH0 air, HC PL APO 20×/0.80 PH2 air, or HC PL APO 40×/0.95 CORR air objectives. Additionally, the microscope was equipped with an LED5 (Leica) or pE-4000 (CoolLED) light source, an incubation chamber, a heated stage, and a CO$_2$ mixer (Pecon). Immunofluorescence stainings were imaged on an inverted wide-field DMi8 microscope (Leica) with an HC PL APO 100×/1.47 oil objective. Imaging data presented in Figs 1 and 4 are available in the external repository "BioImage Archive" EMBL-EBI via "BioStudies" (Sarkans *et al*, 2018) under the accession number S-BIAD901.

Image analysis

Fiji/ImageJ (Schindelin *et al*, 2012) and Imaris (Bitplane) were used for image processing. Generally, only single, noninteracting cells were used for quantification to exclude the influence of neighboring cells on cell path, speed, pore size decision, or the nucleus—MTOC axis. We defined nucleokinesis as intracellular movement of the nucleus for at least one nuclear length relative to cell body, moving from a "losing" protrusion toward a "wining" protrusion.

The overall speed of cells in collagen matrices was analyzed using a custom-made cell tracking tool for ImageJ (Kiermaier *et al*, 2016). In brief, image sequences were background corrected, and particle filtering was used to exclude objects larger or smaller than cells. Each image of the sequence was matched with the optimal overlap in its lateral displacement to the previous frame. Finally, migration velocity was calculated from the y-displacement and the time between two consecutive frames. Speed and distance of nucleus and MTOC in single migrating DCs, T cells, and *Dictyostelium* cells in collagen matrices as well as in pillar forests were analyzed using the manual tracking plugin in Fiji (v2.1.1). Orientation of nucleus and MTOC, as well as nuclear repositioning (whole nuclear body located in losing protrusion followed by full repositioning into winning protrusion), was quantified manually in Fiji.

For the analysis of cells migrating in 1x dead end-channels, the nuclei were tracked using the tracking function of Imaris v9.7.2 with the following settings: object diameter 10 μm, manually adjusted quality threshold, autoregressive motion tracking algorithm (max.

distance 20 μm, gap size = 1). MTOC signals were either tracked manually in Imaris (SPY555-tubulin and EMTB-mCherry) or segmented in ilastik 1.4.0 (Berg *et al*, 2019) (EB3-mCherry) and then tracked using the tracking function of Imaris v9.7.2 with the following settings: object diameter 3 μm, manually adjusted quality threshold, autoregressive motion tracking algorithm (max. distance 25 μm, gap size = 3). Subsequently, all automated tracking was manually evaluated for errors. The cell rear was tracked manually in Imaris. Position data for nuclei and MTOCs were exported and analyzed by a custom-made Matlab script. To accurately associate MTOC tracks with corresponding nuclei, track pairing is achieved by minimizing the convex hull volume between their points. For each nuclear track, the motion direction is calculated, followed by determining the MTOC's distance and orientation relative to the nucleus. To categorize distinct zones within the 1× dead end-channels, their x/y coordinates, and orientations are initially computed using template matching. Subsequently, data from all tracks is consolidated, and maps depicting speed, orientation, and MTOC distance are generated for in-depth analysis.

To analyze retraction dynamics of protrusions with or without nucleus in cells migrating in the 1× dead-end-channels, retraction length, and duration were quantified manually in Imaris.

To measure fluorescence intensities of dextran (10 kDa) coupled to Alexa Fluor™ 647 in the microchannels with competing chemokine and pore size gradients, a rectangular ROI (region of interest) of a defined size was selected on each side of the bifurcation (as indicated in Fig 2B) and the mean intensity was measured over multiple channels. Finally, the fold change was calculated by dividing the mean fluorescence intensity in the "close" channel part by the mean fluorescence intensity in the "distant" channel part.

To visualize the actin and myosin distribution of cells migrating in 1× dead-end-channels, polyline regions of interest were manually drawn on each y-channel separately. The Fiji plug-in kymoreslicewide was then used to create kymographs that show the average of the myosin/actin associated fluorescence over the full width of the microfluidics channels. These kymographs were subsequently transformed from the lab frame of reference to co-moving kymographs. To this end, the cell nuclei were tracked separately with Imaris. The exported center of mass coordinates were used to laterally shift each line of the raw kymographs, so that the nucleus stayed fixed, hence stabilizing the kymograph and yielding the co-moving kymographs of the cells.

Statistics

All replicates were validated independently and represent biological replicates. Samples that did not show migrating cells were excluded. Statistical analysis was conducted using GraphPad Prism using the appropriate tests according to normal or non-normal data distribution as stated in the figure legends. Error bars are defined in the figure legends. No blinding, randomization, and samples size estimations were performed.

Data availability

Imaging data presented in Figs 1 and 4 are available in the external repository "BioImage Archive" EMBL-EBI via "BioStudies" under the accession number S-BIAD901 (https://www.ebi.ac.uk/biostudies/bioimages/studies/S-BIAD901). Computational image analysis scripts are available upon request.

Expanded View for this article is available online.

Author contributions

Janina Kroll: Conceptualization; investigation; methodology; writing – original draft; writing – review and editing. **Robert Hauschild:** Software; writing – review and editing. **Artur Kuznetcov:** Investigation; writing – review and editing. **Kasia Stefanowski:** Investigation; writing – review and editing. **Monika D Hermann:** Investigation; writing – review and editing. **Jack Merrin:** Methodology; writing – review and editing. **Lubuna Shafeek:** Methodology; writing – review and editing. **Annette Müller-Taubenberger:** Resources; writing – review and editing. **Jörg Renkawitz:** Conceptualization; supervision; funding acquisition; investigation; writing – original draft; project administration; writing – review and editing.

Disclosure and competing interests statement

The authors declare that they have no conflict of interest.

References

Andrew N, Insall RH (2007) Chemotaxis in shallow gradients is mediated independently of PtdIns 3-kinase by biased choices between random protrusions. *Nat Cell Biol* 9: 193–200

Barbier L, Sáez PJ, Attia R, Lennon-Duménil A-M, Lavi I, Piel M, Vargas P (2019) Myosin II activity is selectively needed for migration in highly confined microenvironments in mature dendritic cells. *Front Immunol* 10: 747

Berg S, Kutra D, Kroeger T, Straehle CN, Kausler BX, Haubold C, Schiegg M, Ales J, Beier T, Rudy M *et al* (2019) ilastik: interactive machine learning for (bio)image analysis. *Nat Methods* 16: 1226–1232

Bindl J, Molnar ES, Ecke M, Prassler J, Müller-Taubenberger A, Gerisch G (2020) Unilateral cleavage furrows in multinucleate cells. *Cells* 9: 1493

Bornens M (2008) Organelle positioning and cell polarity. *Nat Rev Mol Cell Biol* 9: 874–886

Bouchet BP, Akhmanova A (2017) Microtubules in 3D cell motility. *J Cell Sci* 130: 39–50

Cadot B, Gache V, Gomes ER (2015) Moving and positioning the nucleus in skeletal muscle – one step at a time. *Nucleus* 6: 373–381

Calero-Cuenca FJ, Janota CS, Gomes ER (2018) Dealing with the nucleus during cell migration. *Curr Opin Cell Biol* 50: 35–41

Charras G, Sahai E (2014) Physical influences of the extracellular environment on cell migration. *Nat Rev Mol Cell Biol* 15: 813–824

Clausen BE, Amon L, Backer RA, Berod L, Bopp T, Brand A, Burgdorf S, Chen L, Da M, Distler U *et al* (2022) Guidelines for mouse and human DC functional assays. *Eur J Immunol* https://doi.org/10.1002/eji.202249925

Devreotes PN, Bhattacharya S, Edwards M, Iglesias PA, Lampert T, Miao Y (2017) Excitable signal transduction networks in directed cell migration. *Annu Rev Cell Dev Biol* 33: 103–125

Driscoll MK, Welf ES, Jamieson AR, Dean KM, Isogai T, Fiolka R, Danuser G (2019) Robust and automated detection of subcellular morphological motifs in 3D microscopy images. *Nat Methods* 141: 1–8

Frick C, Dettinger P, Renkawitz J, Jauch A, Berger CT, Recher M, Schroeder T, Mehling M (2018) Nano-scale microfluidics to study 3D chemotaxis at the single cell level. *PLoS ONE* 13: e0198330

Fritz-Laylin LK, Riel-Mehan M, Chen B-C, Lord SJ, Goddard TD, Ferrin TE, Nicholson-Dykstra SM, Higgs H, Johnson GT, Betzig E *et al* (2017) Actin-based protrusions of migrating neutrophils are intrinsically lamellar and facilitate direction changes. *Elife* 6: e26990

Gerisch G, Keller HU (1981) Chemotactic reorientation of granulocytes stimulated with micropipettes containing fMet-Leu-Phe. *J Cell Sci* 52: 1–10

Gundersen GG, Worman HJ (2013) Nuclear positioning. *Cell* 152: 1376–1389

Hadjitheodorou A, Bell GRR, Ellett F, Shastry S, Irimia D, Collins SR, Theriot JA (2021) Directional reorientation of migrating neutrophils is limited by suppression of receptor input signaling at the cell rear through myosin II activity. *Nat Commun* 12: 6619

Hadjitheodorou A, Bell GRR, Ellett F, Irimia D, Tibshirani R, Collins SR, Theriot JA (2023) Leading edge competition promotes context-dependent responses to receptor inputs to resolve directional dilemmas in neutrophil migration. *Cell Syst* 14: 196–209

Hauser MA, Schaeuble K, Kindinger I, Impellizzieri D, Krueger WA, Hauck CR, Boyman O, Legler DF (2016) Inflammation-induced CCR7 oligomers form scaffolds to integrate distinct signaling pathways for efficient cell migration. *Immunity* 44: 59–72

Ishikawa-Ankerhold H, Kroll J, van den Heuvel D, Renkawitz J, Müller-Taubenberger A (2022) Centrosome positioning in migrating dictyostelium cells. *Cells* 11: 1776

Kalukula Y, Stephens AD, Lammerding J, Gabriele S (2022) Mechanics and functional consequences of nuclear deformations. *Nat Rev Mol Cell Biol* 23: 583–602

Kameritsch P, Renkawitz J (2020) Principles of leukocyte migration strategies. *Trends Cell Biol* 30: 818–832

Kay RR, Langridge P, Traynor D, Hoeller O (2008) Changing directions in the study of chemotaxis. *Nat Rev Mol Cell Biol* 9: 455–463

Képiró M, Várkuti BH, Végner L, Vörös G, Hegyi G, Varga M, Málnási-Csizmadia A (2014) para-nitroblebbistatin, the non-cytotoxic and photostable myosin II inhibitor. *Angew Chem Int Ed* 53: 8211–8215

Kiermaier E, Moussion C, Veldkamp CT, Gerardy-Schahn R, de Vries I, Williams LG, Chaffee GR, Phillips AJ, Freiberger F, Imre R *et al* (2016) Polysialylation controls dendritic cell trafficking by regulating chemokine recognition. *Science* 351: 186–190

Kopf A, Renkawitz J, Hauschild R, Girkontaite I, Tedford K, Merrin J, Thorn-Seshold O, Trauner D, Häcker H, Fischer K-D *et al* (2020) Microtubules control cellular shape and coherence in amoeboid migrating cells. *J Cell Biol* 219: e201907154

Krendel M, Zenke FT, Bokoch GM (2002) Nucleotide exchange factor GEF-H1 mediates cross-talk between microtubules and the Actin cytoskeleton. *Nat Cell Biol* 4: 294–301

Kroll J, Ruiz-Fernandez MJA, Braun MB, Merrin J, Renkawitz J (2022) Quantifying the probing and selection of microenvironmental pores by motile immune cells. *Curr Protoc* 2: e407

Lämmermann T, Bader BL, Monkley SJ, Worbs T, Wedlich-Söldner R, Hirsch K, Keller M, Förster R, Critchley DR, Fässler R *et al* (2008) Rapid leukocyte migration by integrin-independent flowing and squeezing. *Nature* 453: 51–55

Leithner A, Eichner A, Müller J, Reversat A, Brown M, Schwarz J, Merrin J, de Gorter DJJ, Schur F, Bayerl J *et al* (2016) Diversified Actin protrusions promote environmental exploration but are dispensable for locomotion of leukocytes. *Nat Cell Biol* 18: 1253–1259

Lomakin AJ, Cattin CJ, Cuvelier D, Alraies Z, Molina M, Nader GPF, Srivastava N, Sáez PJ, Garcia-Arcos JM, Zhitnyak IY *et al* (2020) The nucleus acts as a ruler tailoring cell responses to spatial constraints. *Science* 370: eaba2894

Luxton GG, Gundersen GG (2011) Orientation and function of the nuclear–centrosomal axis during cell migration. *Curr Opin Cell Biol* 23: 579–588

Luxton GWG, Gomes ER, Folker ES, Vintinner E, Gundersen GG (2010) Linear arrays of nuclear envelope proteins harness retrograde actin flow for nuclear movement. *Science* 329: 956–959

Manstein DJ, Titus MA, Lozanne AD, Spudich JA (1989) Gene replacement in dictyostelium: generation of myosin null mutants. *EMBO J* 8: 923–932

Moreau HD, Piel M, Voituriez R, Lennon-Duménil A-M (2018) Integrating physical and molecular insights on immune cell migration. *Trends Immunol* 39: 632–643

Norden C, Young S, Link BA, Harris WA (2009) Actomyosin is the main driver of interkinetic nuclear migration in the retina. *Cell* 138: 1195–1208

Nourshargh S, Alon R (2014) Leukocyte migration into inflamed tissues. *Immunity* 41: 694–707

Pflicke H, Sixt M (2009) Preformed portals facilitate dendritic cell entry into afferent lymphatic vessels. *J Exp Med* 206: 2925–2935

Reinsch S, Gonczy P (1998) Mechanisms of nuclear positioning. *J Cell Sci* 111: 2283–2295

Renkawitz J, Reversat A, Leithner A, Merrin J, Sixt M (2018) Micro-engineered "pillar forests" to study cell migration in complex but controlled 3D environments. *Methods Cell Biol* 147: 79–91

Renkawitz J, Kopf A, Stopp J, de Vries I, Driscoll MK, Merrin J, Hauschild R, Welf ES, Danuser G, Fiolka R *et al* (2019) Nuclear positioning facilitates amoeboid migration along the path of least resistance. *Nature* 568: 546–550

Sarkans U, Gostev M, Athar A, Behrangi E, Melnichuk O, Ali A, Minguet J, Rada JC, Snow C, Tikhonov A *et al* (2018) The BioStudies database—one stop shop for all data supporting a life sciences study. *Nucleic Acids Res* 46: D1266–D1270

Schindelin J, Arganda-Carreras I, Frise E, Kaynig V, Longair M, Pietzsch T, Preibisch S, Rueden C, Saalfeld S, Schmid B *et al* (2012) Fiji: an open-source platform for biological-image analysis. *Nat Methods* 9: 676–682

Schwarz J, Bierbaum V, Merrin J, Frank T, Hauschild R, Bollenbach T, Tay S, Sixt M, Mehling M (2016) A microfluidic device for measuring cell migration towards substrate-bound and soluble chemokine gradients. *Sci Rep* 6: 36440

Schwarz J, Bierbaum V, Vaahtomeri K, Hauschild R, Brown M, de Vries I, Leithner A, Reversat A, Merrin J, Tarrant T *et al* (2017) Dendritic cells interpret haptotactic chemokine gradients in a manner governed by signal-to-noise ratio and dependent on GRK6. *Curr Biol* 27: 1314–1325

Swanson JA, Taylor DL (1982) Local and spatially coordinated movements in *Dictyostelium discoideum* amoebae during chemotaxis. *Cell* 28: 225–232

Thiam H-R, Vargas P, Carpi N, Crespo CL, Raab M, Terriac E, King MC, Jacobelli J, Alberts AS, Stradal T *et al* (2016) Perinuclear Arp2/3-driven Actin

polymerization enables nuclear deformation to facilitate cell migration through complex environments. *Nat Commun* 7: 10997

Tsai L-H, Gleeson JG (2005) Nucleokinesis in neuronal migration. *Neuron* 46: 383−388

van Helvert S, Storm C, Friedl P (2018) Mechanoreciprocity in cell migration. *Nat Cell Biol* 20: 8−20

Venturini V, Pezzano F, Castro FC, Häkkinen H-M, Jiménez-Delgado S, Colomer-Rosell M, Marro M, Tolosa-Ramon Q, Paz-López S, Valverde MA *et al* (2020) The nucleus measures shape changes for cellular proprioception to control dynamic cell behavior. *Science* 370: eaba2644

Weigelin B, Bakker G-J, Friedl P (2012) Intravital third harmonic generation microscopy of collective melanoma cell invasion. *Intravital* 1: 32−43

Wolf K, Alexander S, Alexander S, Schacht V, Schacht V, Coussens LM, Coussens LM, von Andrian UH, van Rheenen J, van Rheenen J *et al* (2009) Collagen-based cell migration models in vitro and in vivo. *Semin Cell Dev Biol* 20: 931−941

Wolf K, Lindert M t, Krause M, Alexander S, Riet J t, Willis AL, Hoffman RM, Figdor CG, Weiss SJ, Friedl P (2013) Physical limits of cell migration: control by ECM space and nuclear deformation and tuning by proteolysis and traction force. *J Cell Biol* 201: 1069−1084

Worbs T, Hammerschmidt SI, Förster R (2017) Dendritic cell migration in health and disease. *Nat Rev Immunol* 17: 30−48

Yamada KM, Sixt M (2019) Mechanisms of 3D cell migration. *Nat Rev Mol Cell Biol* 20: 738−752

Zhu R, Liu C, Gundersen GG (2018) Nuclear positioning in migrating fibroblasts. *Semin Cell Dev Biol* 82: 41−50